From Ce(OH) 3 to Nanoscaled CeO 2 : Identification and Crystal Structure of a Cerium Oxyhydroxide Intermediate Phase

Rémi André, Gwenaëlle Rousse, Capucine Sassoye, Maxim Avdeev, Benedikt Lassalle-Kaiser, Benoît Baptiste, Sophie Carenco

▶ To cite this version:

From Ce(OH)$_3$ to Nanoscaled CeO$_2$: Identification and Crystal Structure of a Cerium Oxyhydroxide Intermediate Phase

Rémi F. André,[1] Gwenaëlle Rousse,[2] Capucine Sassoye,[1] Maxim Avdeev,[3,4] Benedikt Lassalle-Kaiser,[5] Benoît Baptiste,[6] Sophie Carenco,[1,]*

[1] Sorbonne Université, CNRS, Laboratoire de Chimie de la Matière Condensée de Paris (LCMCP), 4 place Jussieu, 75005 Paris, France

[2] Chimie du Solide-Energie, UMR 8260, Collège de France, Paris, France & Sorbonne Université, 4 place Jussieu, 75005 Paris

[3] Australian Nuclear Science and Technology Organisation, Lucas Heights, New South Wales 2234, Australia

[4] School of Chemistry, The University of Sydney, Sydney, New South Wales 2006, Australia

[5] Synchrotron SOLEIL, L'Orme des Merisiers, Départementale 128, 91190 Saint-Aubin, France

[6] Institut de Minéralogie, de Physique des Matériaux et de Cosmochimie (IMPMC), 75005 Paris, France

*Corresponding author. E-mail: sophie.carenco@sorbonne-universite.fr

Abstract

Cerium oxide is a pivotal compound in catalysis, both as support and as active phase. However, its fine features, such as the $Ce^{(III)}$ to $Ce^{(IV)}$ ratio, strongly depend on the protocol used to prepare it. While the literature contains tens of protocols to prepare cerium oxide nanoparticles from $Ce^{(III)}$ precursors, there is still an open question regarding the time at which the cerium oxidation occurs and the role of hydroxide phases in this process. This article identifies an oxyhydroxide phase of $Ce^{(IV)}$ as a key intermediate and proposes a crystal structure for it. In this purpose, phase-pure cerium trihydroxide ($Ce(OH)_3$) nanorods (< 20 nm) were first prepared by hydrothermal treatment of a cerium nitrate salt ($Ce(NO_3)_3 \cdot 6H_2O$) in the presence of KOH. Aging of this phase in air was monitored by X–ray Absorption Spectroscopy (XAS), which confirmed the formation of an intermediate $Ce^{(IV)}$ crystalline compound, unreferenced so far. Based on X–ray and neutron powder diffraction experiments, combined with DFT calculations, we propose that this new phase is a cerium oxyhydroxide of chemical formula $CeO(OH)_2$, for which a structural model is proposed. Thermodiffraction experiments finally established that this compound is an observable intermediate in the synthesis of CeO_2 by the calcination of $Ce(OH)_3$ in air.

1. Introduction

Cerium dioxide (CeO_2) has emerged as a technologically important material during these past decades, with widespread applications in catalysis, both as a support or as the active phase. Applications include vehicle three-way exhaust clean-up, water-gas shift reaction, oxidation of volatile organic compounds or hydrogenation reactions.[1–3] Numerous studies were therefore devoted to the synthesis of cerium oxide nanoparticles (NPs), and to the relation between the size/shape of the nanostructures and the properties of the material, such as redox behavior or oxygen storage capacity, with direct consequences on the performances of the material.[4–7] For practical reasons, a high number of syntheses follow a simple hydrothermal pathway, *i.e.* the treatment of a cerium salt precursor, either $Ce^{(III)}$ (*e.g.* $Ce(NO_3)_3$, $CeCl_3$, $Ce_2(SO_4)_3$) or $Ce^{(IV)}$ (*e.g.* $Ce(NH_4)_2(NO_3)_6$, $Ce(SO_4)_2$), with a precipitating agent (*e.g.* NaOH, KOH, NH_4OH) at moderate temperature (typically 70-200 °C) in water.[8] To do so, a concentrated basic solution is slowly poured into the cerium solution leading to a gradual increase of the pH. On top of the usual safety considerations, such a protocol allows the simultaneous formation of all $Ce(OH)_3$ nuclei, thereby insuring a certain degree of uniformization while limiting aggregation of the particles. In most cases, the synthesis parameters (reagents, temperature, concentrations, reaction time, present ions) allow some control over the shape, size (5–100 nm) and defect density of the nanocrystals.[9] Nevertheless, it must be emphasized that these syntheses are very sensitive to the reaction conditions, as illustrated by the relatively high number of discrepancies and contradictory results in the literature.[8] A full understanding of the formation of CeO_2 NPs by hydrothermal reactions is therefore still unachieved.

The commonly accepted pathway to CeO_2 from $Ce^{(III)}$ salts is the formation of cerium trihydroxide $Ce(OH)_3$ nuclei, which undergo a dissolution–recrystallization process in water upon heating. The oxidation of all $Ce^{(III)}$ species in $Ce^{(IV)}$, required to reach the CeO_2

3

stoichiometric compound, occurs *in situ* thanks to dissolved dioxygen in water.[9] Alternatively, $Ce(OH)_3$ may be isolated as a powder at low temperature, dried and then calcined in air at elevated temperature, typically above 200 °C, to form the CeO_2 oxide. In both cases, several works suggest that the oxidation of cerium occurs first at room temperature with O_2 to form a material denoted $Ce(OH)_4$, which is then dehydrated in CeO_2 upon heat treatment.[10]

The terminology for $Ce(OH)_4$ presents ambiguities as both writings $Ce(OH)_4$ and $CeO_2 \cdot 2H_2O$ may be found in literature and commercial descriptions. Balasubramanian *et al.* showed that this phase has a local structure comparable with that of CeO_2 but is disordered at long range, resulting in an X-ray powder diffraction (XRD) pattern close to that of CeO_2 but with broader peaks.[11] As there is no sharp OH signal observed in Raman spectroscopy, which would be typical of true hydroxides,[12] the authors proposed the term "disordered hydrous cerium oxide" with formula $CeO_2 \cdot xH_2O$, more appropriate than cerium tetrahydroxide $Ce(OH)_4$. *In fine*, according to the comprehensive review of Sorrell *et al.* on ceria syntheses, the only reported crystalline cerium (hydr)oxide phases consist in $Ce(OH)_3$, $Ce(OH)_4$ (or $CeO_2 \cdot xH_2O$), Ce_2O_3, Ce_3O_5, CeO_2 and all the corresponding suboxides.[8,13]

While reproducing a reported protocol for ceria syntheses from literature,[14] we obtained unexpected though reproducible results as to the air aging of the $Ce(OH)_3$ precursor: instead of preserving the $Ce(OH)_3$ crystal phase or obtaining the CeO_2 one, a phase whose XRD pattern is unreferenced was systematically obtained. The aim of the present work is to characterize this phase and propose a crystallographic structure for it. We first present an optimization of the hydrothermal synthesis in order to obtain XRD–pure nanoparticles of cerium trihydroxide ($Ce(OH)_3$) NPs, without any cerium dioxide (CeO_2). Then, the evolution of these $Ce(OH)_3$ NPs upon aging under air is detailed. An intermediate phase is identified for the aged $Ce(OH)_3$, characterized by significant modifications in the XRD pattern and Ce L_{III}-edge X–Ray Absorption Spectroscopy (XAS) signal as compared with $Ce(OH)_3$. Using on

4

one side Rietveld refinements of X–ray and neutron powder diffraction patterns, and on the other side DFT calculations for the hydrogen positions, a crystallographic structure is proposed for the aged $Ce(OH)_3$ with a chemical formula $CeO(OH)_2$ corresponding to an oxyhydroxide of $Ce^{(IV)}$. Finally, *in situ* thermodiffraction experiments were performed to better understand the domain of thermal stability of this new cerium oxyhydroxide phase, and revealed that this latter is an observable intermediate of the calcination of $Ce(OH)_3$ in air, that eventually leads to CeO_2.

2. Results and discussion

2.1. Synthesis of phase-pure cerium trihydroxide $Ce(OH)_3$

In order to gain advanced insights into the formation of CeO_2, it was essential to first obtain a phase-pure $Ce^{(III)}$ precursor. In-depth optimization of a protocol reported by Qu *et al.* was thus the first step of this work.[14] The synthesis of $Ce(OH)_3$ nanoparticles was attempted starting with a nitrate cerium salt ($Ce(NO_3)_3 \cdot 6H_2O$) treated under alkaline conditions, but preliminary results led to a $Ce(OH)_3/CeO_2$ mixture (protocol "CeO_2", see experimental section below).[4] Atmospheric O_2 is known to play a critical role as an oxidant to transform *in situ* the cerium trihydroxide $Ce(OH)_3$ nuclei, formed during the initial mixing of $Ce(NO_3)_3 \cdot 6H_2O$ and NaOH, into CeO_2 nanoparticles.[9] A modified procedure was therefore adopted to prevent such an oxidation, including the deoxygenation of the water by N_2 bubbling. The influence of different parameters was also explored, such as the nature of the reaction vessel (Nalgene *vs.* air-tight Pyrex), the nature of the precipitating agent (NaOH *vs.* KOH), its concentration, the reaction temperature (75 °C *vs.* 100 °C), the nature of the gas phase in the vessel (air *vs.* N_2), the filling level of the vessel, the reaction time and finally the nature of the cerium source ($Ce(NO_3)_3 \cdot 6H_2O$ *vs.* $CeCl_3$). All the results are presented in supporting information (section SI B, **Table S1** and **Figure S2)**, and the following conditions were chosen in order to

minimize the amount of CeO_2: air-tight Pyrex vessel, $[KOH] = 4.3$ M, $[Ce(NO_3)_3 \cdot 6H_2O] = 0.05$ mol.L^{-1}, T $= 100$ °C, under N_2 with vessel filled at 55 % (**Table S1**, entry 12). The robustness of the synthesis of $Ce(OH)_3$ should nonetheless be highlighted as this phase was obtained over a wide range of reaction conditions, with a similar crystallite size of *ca.* 8 nm, estimated from Scherrer analysis.

As expected, the gas phase of the reaction (air *vs.* N_2) was the parameter with the strongest impact. Assuming that the oxidation of $Ce(OH)_3$ into CeO_2 occurred according to *Eq. 1* (below), four cerium atoms were oxidized per available O_2 molecule. Dioxygen has a limited solubility in water $([O_2]_{max} = 0.28$ $mM^{15})$ at room temperature so, with the current procedure $([Ce] = 0.05$ M), only 2 % of the $Ce^{(III)}$ could be oxidized in $Ce^{(IV)}$, in agreement with the marginal formation of CeO_2 in absence of air. The contribution of dissolved O_2 could therefore be neglected in a first approach and the deoxygenation of water was probably not crucial to limit the formation of CeO_2. On the contrary, the amount of CeO_2 produced increased in the presence of atmospheric O_2. (**Table S1**, entry 14). The available amount of O_2 in the gas phase in the vessel, taking into account the concentration of O_2 in air of *ca.* 20 %, is given by *Eq. 2* with $V_{mol} = 24.05$ L.mol^{-1}. In case $V_{reaction} = 12$ mL for a vessel of volume $V_{vessel} = 66$ mL (filling level of 18 %, entry 9), the amount of dioxygen, $n(O_2) = 0.44$ mmol, largely exceeded that theoretically required to oxidize all the cerium atoms $(n(Ce) = 0.6$ mmol), yet CeO_2 was a minor phase. We therefore concluded that the oxidation of $Ce(OH)_3$ into CeO_2 could not be complete if the consumption of dioxygen led to a large decrease of the partial pressure in the gas phase in the vessel. This explained the need to renew the gas phase with fresh air to reach a complete oxidation.

$$4 \, Ce(OH)_3 \; + \; O_2 \; \rightarrow \; 4 \, CeO_2 \; + \; 6 \, H_2O \qquad\qquad (1)$$
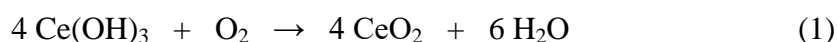
$$n(O_2) = 0.2 \, (V_{vessel} - V_{reaction})/V_{mol} \qquad\qquad (2)$$

Taking into consideration all the mentioned parameters, an optimized $Ce(OH)_3$ synthesis could be proposed (**Figure 1A** and protocol "$Ce(OH)_3$", see experimental section below). The powder was extensively washed with water until neutral pH was reached, and it was then dried. One may not formally exclude the presence of potassium ion leftovers at the surface of the nanoparticles, as well as other atoms such as Si, leached from the borosilicate glass (see SI). However, these impurities are expected to be in limited contents. Water is indeed the standard solvent used for washing CeO_2 NPs and, to the best of our knowledge, there is no report of a significant crystallographic rearrangement in the bulk of the NPs due to the incorporation of ions from the reaction medium.[8] The sample was sealed in a glass capillary and its diffraction pattern was recorded at the CRISTAL beamline of synchrotron SOLEIL. The Rietveld refinement confirms that the material was composed of $Ce(OH)_3$ with space group $P\,6_3/m$ and lattice parameters $a = 6.48977(5)$ Å and $c = 3.79798(3)$ Å, in agreement with previous reports (**Figure 1B** and **Table 1, top**).[13] An anisotropic size broadening was introduced as spherical harmonics and revealed needle-like crystallites of 15 nm long (along [001]) and 5 nm diameter (**Figure 1C**). Note that this was consistent with the shape observed by Transmission Electron Microscopy (TEM) that revealed polydisperse nanorods: the average length was 100 nm for a mean width of 10 nm (**Figure 1D**). These nanorods were therefore built on a few crystallites. Selected Area Electron Diffraction (SAED) was collected on a few nanorods (**Figure 1E**). Indexation of the diffraction rings was consistent with the presence of $Ce(OH)_3$. This supported the phase attribution proposed on the basis of the XRD pattern. Moreover, this observation by SAED testified of the stability of the trihydroxide under high vacuum, at least for a few tens of minutes.
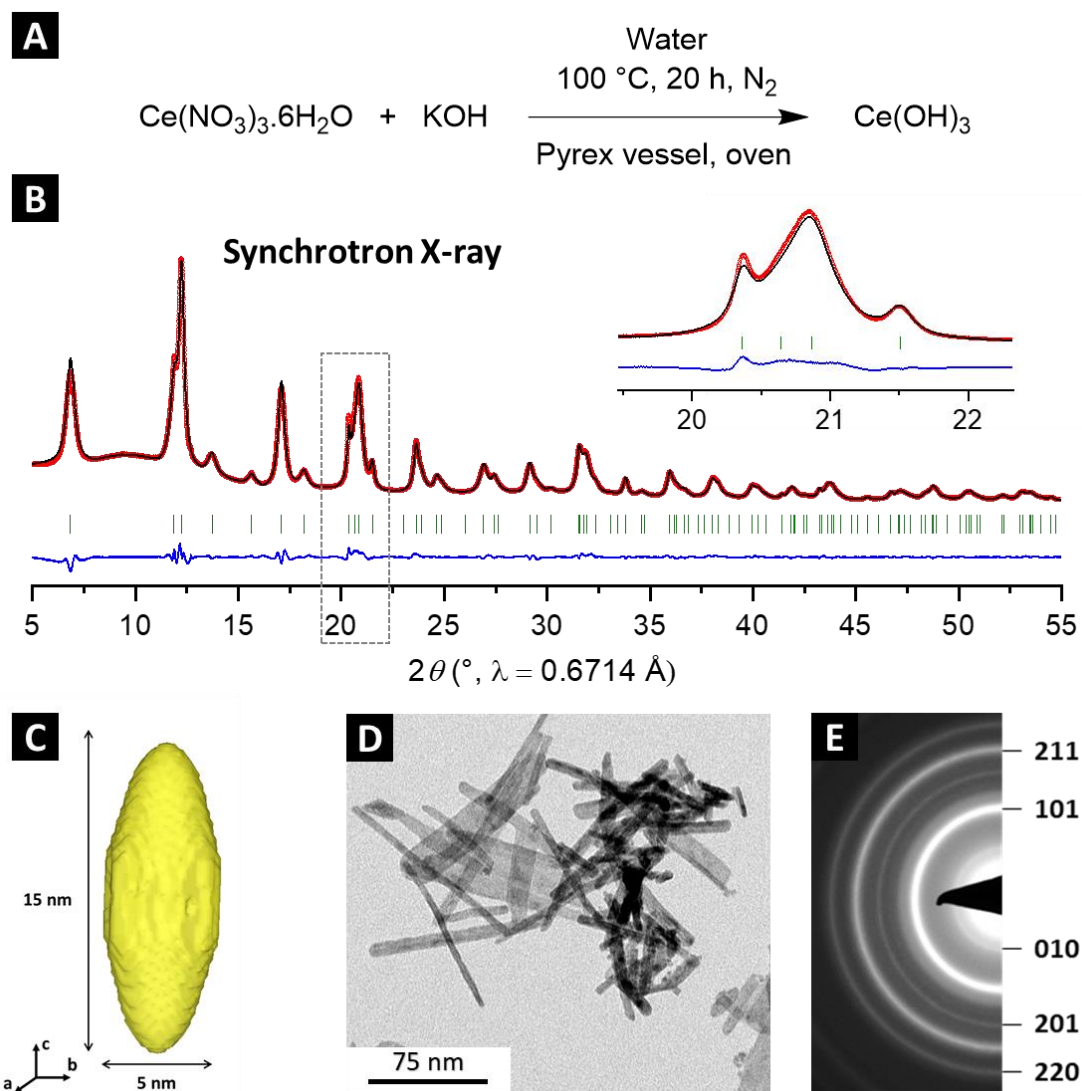
Figure 1. Hydrothermal synthesis of Ce(OH)₃ nanoparticles. (A) Reaction conditions. (B) Rietveld refinement XRD pattern (red: experimental data, black: calculated pattern, blue: difference, green bars: Bragg positions) with zoom on the [20-22]° region. (C) Shape of the crystallites as deduced from the Rietveld refinement. (D) TEM image and (E) corresponding SAED pattern.

Ce(OH)$_3$ 300 K	$P\,6_3/m$			R_{Bragg} = 2.81 %	χ^2 = 16.6
a = 6.48977(5) Å				c = 3.79798(3) Å	Vol = 138.530(2) Å^3

Atom	Wyckoff Position	x/a	y/b	z/c	B_{iso} (Å^2)	Occupancy
Ce1	2c	1/3	2/3	1/4	0.9439(16)	1
O1	6h	0.3666(3)	0.2900(3)	1/4	1.79(3)	1

CeO(OH)$_2$ 300 K	$P\,2_1/m$			R_{Bragg} = 1.44 %	χ^2 = 7.83
a = 6.03502(14) Å	b = 3.62918(3) Å β = 120.4117(14)°			c = 6.24254(9) Å	Vol = 117.913(3) Å^3

Atom	Wyckoff Position	x/a	y/b	z/c	B_{iso} (Å^2)	Occupancy
Ce1	2e	0.68884(6)	1/4	0.33581(10)	1.1207(16)	1
O1	2e	0.2630(9)	1/4	0.3206(8)	3.29(4)	1
O2	2e	0.6121(10)	1/4	-0.0961(8)	3.29(4)	1
O3	2e	0.0728(7)	1/4	0.6913(7)	3.29(4)	1
H1	2e	0.08935	1/4	0.18048	2.0	1
H2	2e	0.74868	1/4	0.86501	2.0	1

Table 1. Crystallographic data and atomic positions for Ce(OH)$_3$ (top) and CeO(OH)$_2$ (bottom) at 300 K using the complete model determined from Rietveld refinement of the synchrotron X–ray patterns. The positions of the two hydrogen atoms in CeO(OH)$_2$ are those by DFT calculations, and were not refined.

2.2. Oxidation of cerium trihydroxide Ce(OH)$_3$ upon aging in air

The obtained Ce(OH)$_3$ material evolved over time when stored in air: while the fresh powder was grey, it gradually turned yellow. A clear evolution upon aging was also observed on the XRD pattern: peaks tended to decrease until disappearance while new peaks (often with modified shape) appeared with a shift towards the high angles (**Figure 2**). On the contrary, when the material was stored in argon, neither the material color nor the diffraction pattern did significantly evolve: the aging only occurred in the presence of O$_2$, presumably as an oxidizing agent. Based on the intensity of the peaks at 40° and 41.9°, the timescale of the material evolution in air was evaluated to be three days (**Figure 2**, inset). Attribution of the reflections was not trivial because all the CeO$_2$ diffraction peaks [ICDD N°00-034-0394] were located beneath those of Ce(OH)$_3$ [ICDD N°00-055-0556]. Thus, the presence of CeO$_2$ in fresh Ce(OH)$_3$ samples cannot be excluded *a priori*. It is however easier to exclude CeO$_2$ from the analysis of the evolved Ce(OH)$_3$. Even after 6 months of storage in air at r.t., batches strictly free from CeO$_2$ were indeed obtained (**Figure S3**), indicating that the aged Ce(OH)$_3$ was stable under ambient conditions. Upon aging, the morphology of the NPs did not evolve according to TEM (**Figure S4A**). On the contrary to fresh Ce(OH)$_3$ and CeO$_2$, aged Ce(OH)$_3$ suffered from electron beam damages, presumably due to the heat produced by the electron beam (**Figure S4B**). An electron diffraction pattern could nonetheless be registered before decomposition and was consistent with the evolution of the X–ray diffraction pattern as a dilatation of the rings, *i.e.* a contraction of the interplanar distances in the crystalline structure, was detected (**Figure S5** and **Table S2** for X–ray and electron diffraction comparison).
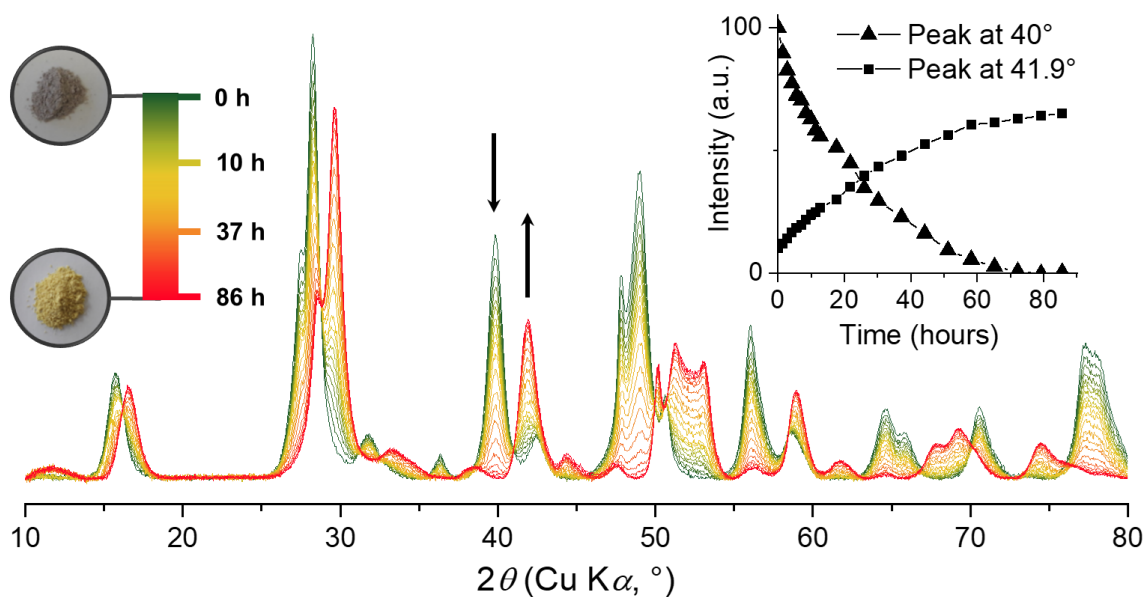
Figure 2. X–ray diffractograms of Ce(OH)$_3$ during aging in air. Inset: intensity of the (201) peak of Ce(OH)$_3$ (at 40°) and aged Ce(OH)$_3$ (at 41.9°) with time.

To the best of our knowledge, all the articles mentioning the aging of Ce(OH)$_3$ NPs in air reported a final phase with a fluorite-like cubic structure. For instance, Golberg *et al.* synthesized Ce(OH)$_3$ nanotubes by hydrothermal treatment of CeCl$_3$ with a 12 M NaOH solution in an autoclave between 100 °C and 150 °C.[16] The obtained nanotubes, several hundred nanometers long, were exposed to air for several days under ambient conditions and the material evolved into the cubic CeO$_2$ with broad diffraction peaks, attributed to the local disorder due to hydration by water molecules. For comparison, these reaction conditions (CeCl$_3$, 120 °C, 12 M NaOH in autoclave) were reproduced here and Ce(OH)$_3$ was also obtained, albeit with larger crystallite size of *ca.* 25 nm (**Table S1**, entry 17). The XRD pattern of the material reproduced according to Golberg's conditions recorded after three days in air did not exhibit any peak corresponding to the unreferenced phase observed in **Figure 2**. A PXRD pattern similar to our "aged Ce(OH)$_3$" was nonetheless reported by Qu *et al.*, though no convincing phase attribution could be proposed.[14,17] As no phase could match the XRD

powder pattern in neither the ICSD nor the ICDD databases, the following section is devoted to the structural determination of the aged Ce(OH)$_3$ phase.

2.3 Structure proposal for a cerium oxyhydroxide phase: CeO(OH)$_2$

X–ray Absorption Spectroscopy (XAS). Considering the striking color change occurring upon exposure to air (from grey to yellow), the oxidation state (o.s.) of the cerium atoms was expected to increase from +III to +IV and was therefore investigated by XAS at the Ce L$_{III}$-edge. Figure 3 displays the XAS spectra of pellets of commercial Ce(NO$_3$)$_3$·6H$_2$O (orange), commercial CeO$_2$ (blue), CeO$_2$ nanorods (dark green), fresh (red) and aged Ce(OH)$_3$ (light green). The edge positions indicate that aged Ce(OH)$_3$ (5725.8 eV) has the same average Ce o.s. as commercial CeO$_2$ (5725 eV) and CeO$_2$ nanorods (5725.4 eV), *i.e.* mostly Ce$^{(IV)}$. Cerium nitrate, an air-stable Ce$^{(III)}$ salt, and fresh Ce(OH)$_3$ (measured before any exposure to air) have an edge at a lower energy (respectively 5723.3 eV and 5723.4 eV), consistent with a lower o.s.[18]

Overall, upon aging under air of Ce(OH)$_3$ NPs, the edge shifts towards higher energies, which suggests a quantitative oxidation of Ce$^{(III)}$ in Ce$^{(IV)}$. It should be noted that aged Ce(OH)$_3$ may have suffered from beam damage, resulting in some dehydratation and/or the formation of some amount of CeO$_2$. On the other hand, the X-ray beam did not oxidize the two other Ce$^{(III)}$ compounds: Ce(NO$_3$)$_3$·6H$_2$O and fresh Ce(OH)$_3$. Thus, we consider that the observation of Ce$^{(IV)}$ species in the aged Ce(OH)$_3$ is mostly due to the aging in air, and not to an effect of the beam.
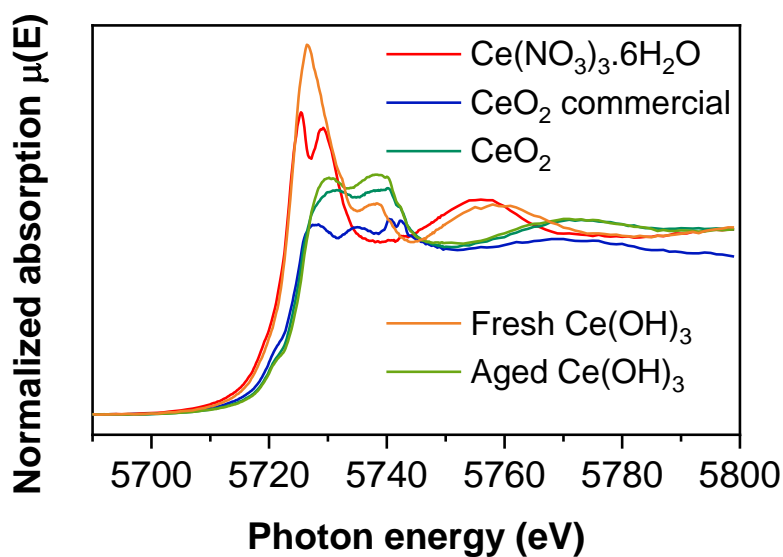
**Figure 3.** Ce L_{III}-edge XAS spectra of commercial Ce(NO$_3$)$_3$·6H$_2$O, commercial CeO$_2$, CeO$_2$ nanorods, and of fresh and aged Ce(OH)$_3$, measured as pellets in graphite.

Rietveld refinement. The structural determination of aged Ce(OH)$_3$ was undertaken from the synchrotron X-ray diffraction pattern of the aged powder sealed in a glass capillary, *i.e.* in the same conditions as the pattern of the fresh Ce(OH)$_3$ (**Figure 1**). The similarity between the fresh and aged Ce(OH)$_3$ patterns indicates that there is a structural relationship between both compounds. Our initial trials to index the aged Ce(OH)$_3$ pattern in the same symmetry (space group $P\,6_3/m$) but with smaller lattice parameters to account for the shift of peaks towards higher angles led to an unsatisfactory fit for some reflections which appear split compared to a hexagonal symmetry, for instance in the $2\theta = [21\text{-}23]°$ region. Therefore, attempts were made in the maximal non-isomorphic subgroups of $P\,6_3/m$, with the help of the Isodistort program.[19,20] Among all possibilities, the subgroup $P\,2_1/m$ with lattice parameters $a = 6.03502(14)$ Å, $b = 3.62918(3)$ Å, $c = 6.24254(9)$ Å and $\beta = 120.4117(14)°$, can successfully index the pattern, with a particularly good fit on the $2\theta = [21\text{-}23]°$ region where splitting strongly occurs and many peaks overlap (see inset of **Figure 4A**). This monoclinic unit cell can be related to the hexagonal one by the following relation between lattice vectors (the indexes m and h refer to the monoclinic and hexagonal lattice vectors, respectively):

13

$$\begin{pmatrix} \boldsymbol{a_m} \\ \boldsymbol{b_m} \\ \boldsymbol{c_m} \end{pmatrix} = \begin{pmatrix} 0 & 1 & 0 \\ 0 & 0 & 1 \\ 1 & 0 & 0 \end{pmatrix} \begin{pmatrix} \boldsymbol{a_h} \\ \boldsymbol{b_h} \\ \boldsymbol{c_h} \end{pmatrix}$$

A structural model in the monoclinic cell was then derived from the positions of Ce and O atoms in hexagonal $Ce(OH)_3$, and these atoms were freely refined against the synchrotron pattern resulting in the refinement shown in **Figure 4A**. At this stage, it should be noted that while this structural model confirmed the Ce:O ratio (1:3), it still needs to be reconciled with XAS spectroscopy which indicated o.s. of +IV: charge developed on Ce has to be compensated for the material to remain neutral. We suggest that the oxidation of $Ce^{(III)}$ into $Ce^{(IV)}$ by dissolved O_2 leads to the solid departure of proton through H_2O as detailed in *Eq. 3*. Such a mechanism would be consistent with an increased stability of larger $Ce(OH)_3$ crystallites due to a slower diffusion of O_2 and H_2O in the crystal, as experimentally observed (our conditions *vs.* Golberg's conditions).

$$2\ Ce(OH)_3\ +\ \tfrac{1}{2}\,O_2\ \rightarrow\ 2\ CeO_3H_2\ +\ H_2O \tag{3}$$
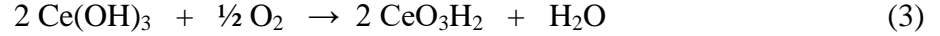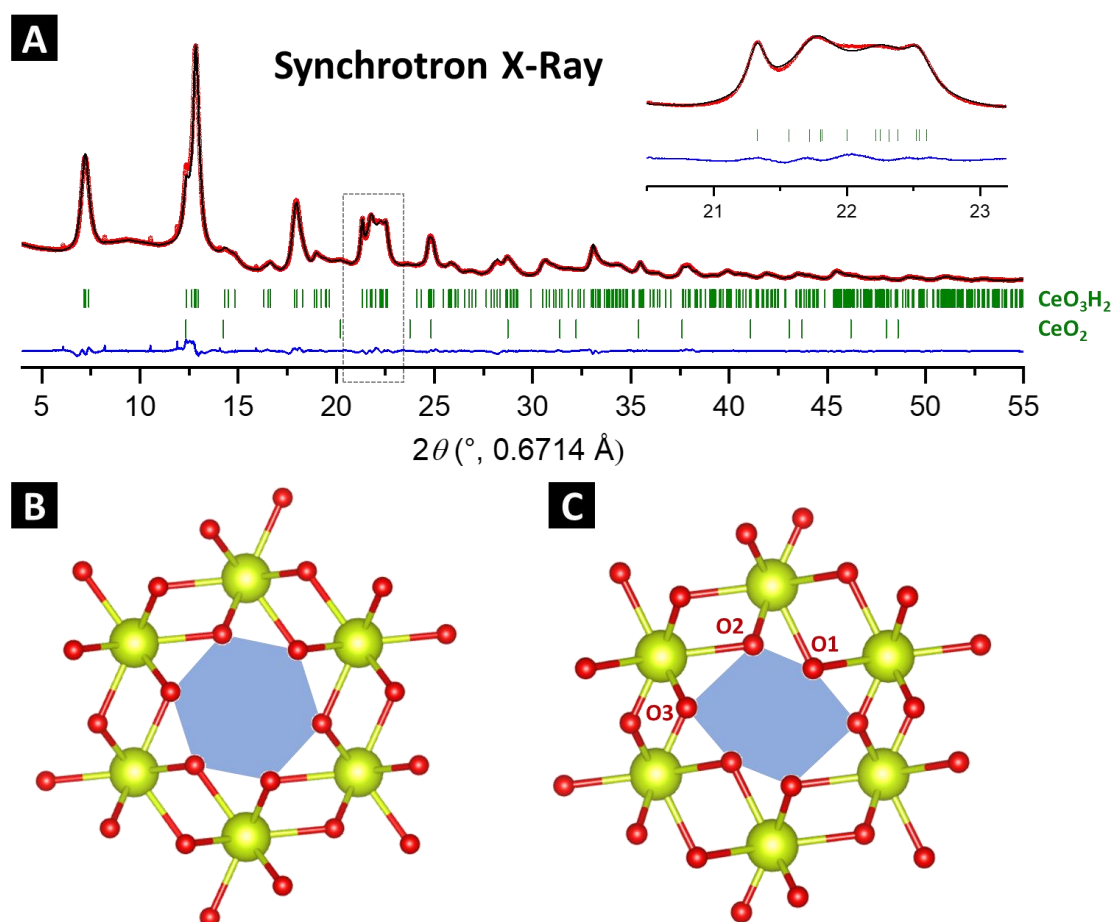
Figure 4. Rietveld refinements of the cerium hydroxide aged in air. (A) Rietveld refinement XRD pattern (red: experimental data, black: calculated pattern, blue: difference, green bars: Bragg positions) with zoom on the [21-23]° region. (B, C) Crystal structures of the CeO_3 skeleton of respectively $Ce(OH)_3$ and CeO_3H_2 (Ce and O are represented as yellow and red balls, respectively). Blue hexagons delineate the base of the formed channels.

The CeO_3H_2 chemical formula can be understood as $CeO(OH)_2$, *i.e.* the evolution of a hydroxo anion HO^- in an oxo one O^{2-}, or as $CeO_2(H_2O)$ for which Ce is not connected to two hydroxyl groups but to a water molecule. Although the CeO_3 skeleton can clearly be identified by synchrotron X-ray diffraction, the scattering difference between O^{2-}, HO^- and H_2O is not straightforward and the positions of eventual hydrogen atoms are almost impossible to assess using XRD.

We therefore performed Neutron Powder Diffraction (NPD) experiments. The aged $Ce(OH)_3$ powder, prepared as a large batch for which we could not avoid CeO_2 traces (see

15

Figure S6 for the corresponding XRD pattern), was sealed in a vanadium can and the diffraction pattern was measured at room temperature with a wavelength of 1.622 Å. The nano scale of the crystallites and the large incoherent scattering of hydrogen atoms makes the pattern difficult to analyse and the quality of the pattern prevents locating hydrogen atoms by difference Fourier maps (**Figure 5A**).

To overcome this difficulty, DFT calculations were used to propose a structural model that can be validated by neutrons. Both the oxyhydroxide $CeO(OH)_2$ (model 1) and hydrate $CeO_2(H_2O)$ (model 2) were considered. For the model 1 (oxyhydroxide $CeO(OH)_2$), H atoms were sequentially placed at each point of a three-dimensional grid covering the unit cell with step 0.2 Å and the total energy was calculated. The points corresponding to the lowest total energy corresponded to the positions most energetically favorable for H atoms. Full structure geometry optimization was further performed starting with H atoms placed in those locations. For the model 2 (hydrate $CeO_2(H_2O)$), first the largest voids suitable to host water molecules were located using *MedeA* software built-in tools based on Voronoi partitioning. Further, water molecules were placed in the voids in random orientations and their orientation optimized using DFT. Multiple starting random orientations were tested and all converged to the same final atom positions. The DFT calculations consistently showed that oxyhydroxide $CeO(OH)_2$ is more stable than hydrate $CeO_2(H_2O)$ by ~1 eV/unit cell.

The structural model presenting the lowest energy of the model 1 ($CeO(OH)_2$) corresponds to hydrogen atoms linked to O1 and O2 so as to form hydroxo anions (**Figure 5B**). The second model corresponds to both hydrogens atom linked to O1 so as to form a structural water molecule, also developing a hydrogen bond with the vicinal oxygen O2 atoms (**Figure 5C**). Although the quality of the NPD data did not allow to directly locate H atoms via difference Fourier maps, the NPD pattern simulated for the model 1 is closer to the experimental data, especially considering the peaks at 44° and 66° (**Figure 5A**), and is more

probable as predicted to be more stable by DFT. Better crystallized compounds with larger crystallite size would be necessary to confirm the crystal structure by NPD.

Table 1, bottom lists the lattice parameters and atomic positions of $CeO(OH)_2$, with Ce and O deduced from the synchrotron Rietveld refinement and H from the DFT calculations. A comparison of the PXRD patterns with the referenced peak positions for CeO_2 and $Ce(OH)_3$, and of the calculated ones for $CeO(OH)_2$ is given in **Figure S7**. As for $Ce(OH)_3$, Ce is surrounded by 9 oxygen atoms forming a distorted tri-capped trigonal prism, the typical coordination polyhedron of AX_9 geometries. The oxygen atoms form a hexagon (delineated in blue in **Figure 4B-C**) at the basis of channels in the extended structure (**Figure S8**). Compared to $Ce(OH)_3$, the hexagonal-shaped tunnels are flattened because of the monoclinic distortion. This subtle flattening occurs along the O3–O3 axis. The O3 oxygen atoms are indeed the only ones that are O^{2-}, as opposed to O1 and O2 which are hydroxyl oxygen (model $CeO(OH)_2$), or O1 which is a water molecule and O2 which benefits from hydrogen bonding (model $CeO_2(H_2O)$): O3 therefore generates the highest electrostatic repulsion between the two diametrically opposed oxygens, as these are not screened by hydrogens, hence the elongation.
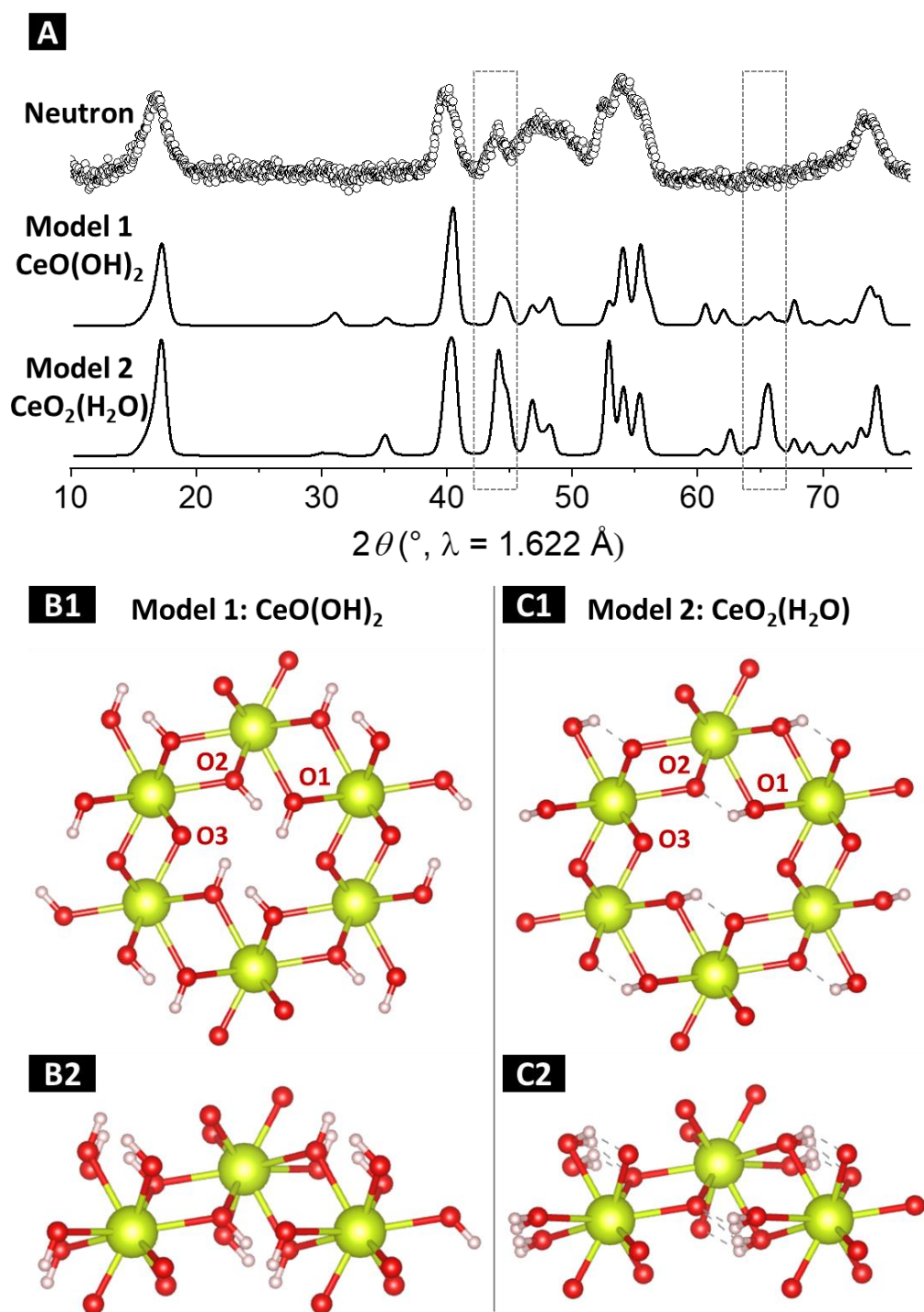
Figure 5. (A) Neutron Powder Diffraction (NPD) data of aged Ce(OH)$_3$ (up) and calculated patterns for models 1 (middle) and 2 (bottom). Acquisition at a wavelength of 1.622 Å. Crystal structures of (B) model 1 CeO(OH)$_2$ and (C) model 2 CeO$_2$(OH), viewed along c-axis (B1, C1) or from a tilted angle (B2, C2) (Ce, O and H are represented as yellow, red and white balls, respectively, and dotted lines indicate H–bonding).

Infrared spectroscopy. Attenuated Total Reflectance-Fourier Transform InfraRed (ATR-FTIR) analysis was finally performed in an attempt to probe the nature of the O–H bonds inside the structures (**Figure 6A**). In fresh $Ce(OH)_3$ (spectrum (a)), O–H and Ce–O stretching bands, both specific of the metal hydroxide phases, were detected at respectively 3606 cm^{-1} and 650 cm^{-1} (**Figure 6B–C**).[21,22] Upon aging, the two absorption bands split in two, lost intensity and shifted in energy at 3597/3586 cm^{-1} and 741/713 cm^{-1} (spectrum (b)), which may be the mark of a loss of symmetry in the crystal structure, or of the presence of chemically different oxygen sites. The shift towards higher energies for the Ce–O bond absorption band can be understood as a strengthening of the chemical bond due to a higher o.s. of the cerium center. The spectrum of CeO_2 (spectrum (c)) did not display any thin peak in the O–H region though it was exposed to air so the thin peaks at *ca.* 3600 cm^{-1} observed in spectra (a-b) cannot be explained only by surface hydroxyl species but indeed by structural water molecules or bulk hydroxyl groups. The bands between 1600 cm^{-1} and 1300 cm^{-1} are attributed to scissoring mode of adsorbed H_2O and C=O stretching of surface carbonate CO_3^{2-} species, atmospheric CO_2 being easily adsorbed on metal oxides and hydroxides.[23,24] The intense and broad band at 1000 cm^{-1} observed in spectra (a-b) could not be attributed. Finally, the absorption bands in aged $Ce(OH)_3$ did not match with those of commercial cerium tetrahydroxide ($Ce(OH)_4$) (spectrum (d)) which presented complex features in the O–H region (3000–3600 cm^{-1}) and a large band at 1300 cm^{-1}. Such a striking difference suggests the absence of hydration water molecule, as described for $Ce(OH)_4$, in the aged $Ce(OH)_3$ material.
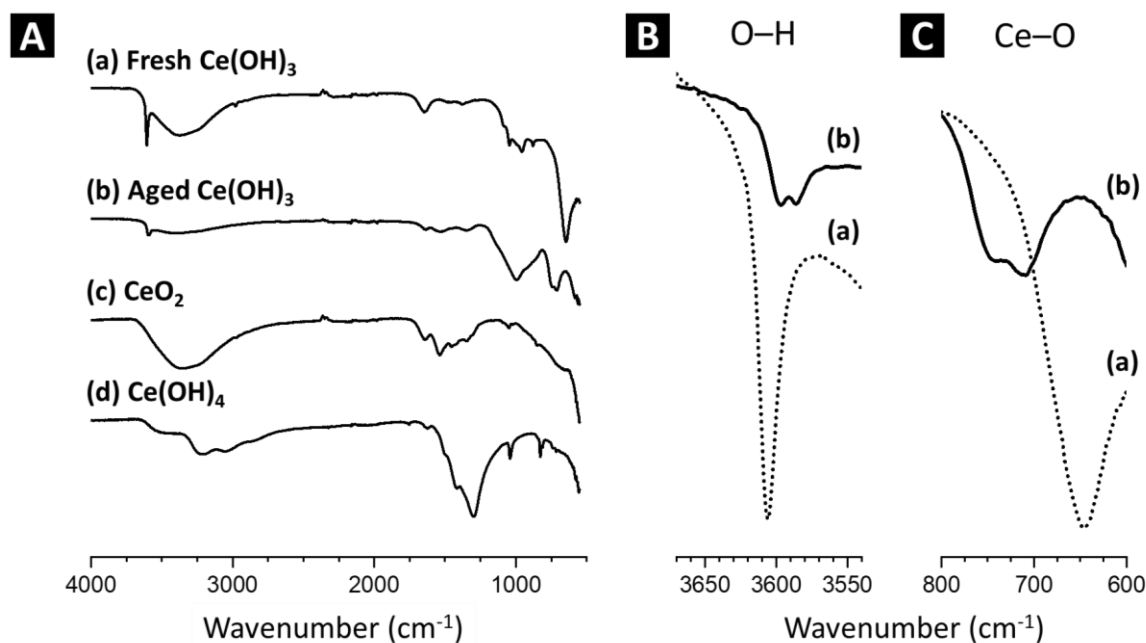
**Figure 6.** (A) ATR-FTIR spectra of (a) fresh $Ce(OH)_3$, (b) aged $Ce(OH)_3$, (c) CeO_2 and (d) commercial $Ce(OH)_4$. Zooms on the (B) O–H and (C) Ce–O regions.

2.4. *In situ* formation of CeO_2 from $Ce(OH)_3$ and $CeO(OH)_2$ upon calcination in air

As previously mentioned, cerium dioxide NPs are commonly prepared starting from a $Ce^{(III)}$ precursor *via* an *in situ* generated $Ce(OH)_3$ phase. The transformation of this last one into CeO_2 therefore implies both an oxidation of the cerium center and a dehydration with the loss of water molecules. We have already demonstrated the oxidation of $Ce^{(III)}$ in $Ce^{(IV)}$ may occur under ambient conditions without total dehydration for small NPs. In order to monitor this process, the calcination in air of both $Ce(OH)_3$ and $CeO(OH)_2$ was therefore studied by *in situ* thermodiffraction. The powders were treated with an average heating ramp of 10 °C/h from r.t. to 150 °C while recording X–ray powder patterns every 5 °C (**Figure 7**). Phase attributions can be checked on **Figures S9-10** for the different regimes. When starting from $CeO(OH)_2$, the material was stable up to 75 °C and then rapidly underwent a transformation into CeO_2 (**Figure 7A**). For $Ce(OH)_3$, the $CeO(OH)_2$ phase was obtained between 50 °C and 75 °C and the CeO_2 phase was obtained above (**Figure 7B**). The FTIR spectrum of $CeO(OH)_2$

calcined at 200 °C accordingly evolved to correspond to the spectrum of CeO_2, to the exception of the previously mentioned unattributed band at 1000 cm^{-1} (**Figure S10**). This experiment confirmed that the $CeO(OH)_2$ phase is a reaction intermediate from $Ce(OH)_3$ to CeO_2.
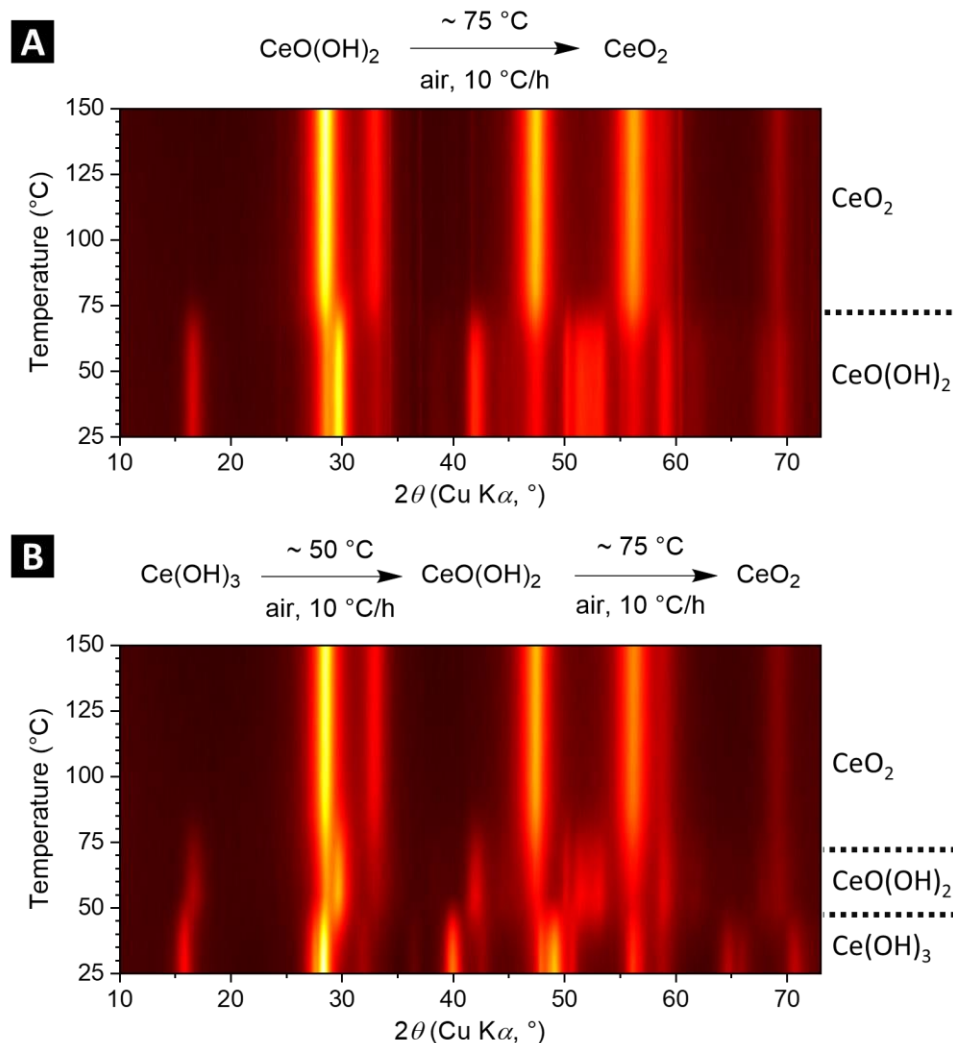
Figure 7. *In situ* **thermodiffraction experiments performed in air at a heating rate of 10 °C/h:** calcination of (A) $CeO(OH)_2$ and (B) $Ce(OH)_3$.

It clearly appears from the thermodiffraction experiments that the two steps, (1) oxidation of cerium in air and (2) crystallographic rearrangement and dehydration, are not simultaneous and that oxidation occurs first. The threshold temperature of 50 °C, observed for the transformation $Ce(OH)_3 \rightarrow CeO(OH)_2$, naturally depends on the experimental condition

(temperature, heating rate) as the same oxidation occurs at r.t. in a few days. The displacement of the atoms from the pseudo-6-fold symmetry structure of $CeO(OH)_2$ towards the fluorite one, associated with the loss of a water molecule, may thus be considered as the limiting step of the formation of the CeO_2 phase. Considering that most of the reported protocols for CeO_2 synthesis include a final drying step in an oven at *ca.* 60 °C, the oxyhydroxide phase may be transformed into CeO_2 before the diffractograms are recorded, explaining the lack of characterization of $CeO(OH)_2$ so far.

It is noteworthy that, when $Ce(OH)_3$ was calcined under argon at 200 °C during 2 h, no structural modification was observed on the XRD pattern (**Figure S11**), nor on the FTIR spectrum (**Figure S12**). This absence of evolution highlights the importance of the oxidation of the cerium atoms to trigger the dehydration in CeO_2. Even though the formation of CeO_2 from $Ce(OH)_3$ was reported by Golberg *et al.* at 450 °C in an ammonia atmosphere,[16] no data could be found as to lower temperature experiments in absence of an oxidative atmosphere.

3. Conclusion

While synthesizing cerium dioxide NPs *via* cerium trihydroxide NPs, an unreported XRD pattern was systematically obtained upon aging of $Ce(OH)_3$ in air, corresponding to a compound stable over months. A deeper look at the literature revealed that such a material, obtained here by serendipity, has already been encountered in similar studies and that difficulties appeared as to its phase attribution. On the basis of XRD, this unreported "aged $Ce(OH)_3$" phase clearly differed from the most commonly reported cerium-containing phases, *i.e.* cerium dioxide (CeO_{2-x}), cerium sesquioxide (Ce_2O_3), and hydrous cerium oxide/cerium tetrahydroxide ($CeO_2 \cdot x H_2O / Ce(OH)_4$). A structural study with Rietveld refinement of X-ray and neutron powder diffraction, complemented by XAS and IR data as well as DFT calculations, enabled us to propose a new structure for this cerium oxyhydroxide phase.

Additionally, *in situ* thermodiffraction experiments showed that this cerium oxyhydroxide transformed into fluorite-type CeO_2 in air at relatively low temperature (75 °C). Moreover, the cerium oxyhydroxide phase was also observed as an intermediate during the calcination of $Ce(OH)_3$ into CeO_2 in air. So far, the results suggest the formation of this oxyhydroxide phase is straightforward only for small nanoparticles (< 10 nm). We believe such findings will be helpful to the material community in quest of a better understanding of cerium dioxide NPs formation, as well as of the stability and redox properties of this crucial material.

4. Experimental section

Chemicals. All chemicals were used as received without further purification. $Ce(NO_3)_3 \cdot 6H_2O$ (99.5 %) (main impurity: La), NaOH (98 %) and KOH (85 %) (main impurity: H_2O) were purchased from Alfa Aesar, $CeCl_3$ (98 %) from Fluka, CeO_2 (99.9 %) from Merck, $Ce(OH)_4$ (85 %) from Strem Chemicals and the ethanol (96 %) from VWR. Distilled water was prepared using a Merck Milli-Q system (25 MΩ.cm). No trace of La-containing phase such as La_2O_3 was detected in this study.

Synthesis of cerium dioxide CeO_2. In a 250 mL Nalgene vessel, 3.91 g of $Ce(NO_3)_3 \cdot 6 H_2O$ (9 mmol, 1 equiv.) were dissolved in 30 mL of distilled water to yield a colorless limpid solution. Meanwhile, 43 g of NaOH pellets (1.075 mol, 6 M) were dissolved in 150 mL of water and the resulting solution was slowly added to the cerium nitrate solution. A yellow-brown precipitate appeared at the first drops, followed by a yellow gel and a grey gel and finally a violet suspension. The turbid violet solution was stirred 30 min and was then put in a preheated electric oven at 100 °C for 20 h. After reaction, the solution was let to cool down naturally to r.t. A grey-violet powder sedimented at the bottom of the vessel, the supernatant was colorless. The whole suspensions were brought together and centrifugated (9,000 rpm, 10 min, 20 °C). The grey powder was washed 6 times with 30 mL of H_2O and

once with 30 mL of EtOH: along the washings, the powder gradually turned beige. The obtained beige powder (1.45 g, 94 % yield) was then dried under N_2 and stored under air.

Optimized synthesis of cerium trihydroxide Ce(OH)₃. In a 66 mL Pyrex vessel and under a flux of N_2, 780 mg of $Ce(NO_3)_3 \cdot 6\,H_2O$ (1.8 mmol, 1 equiv.) were dissolved in 6 mL of water, deoxygenated by N_2-bubbling during 4 h, to yield a colorless limpid solution. Meanwhile, 8.64 g of KOH (154 mmol) were dissolved in 30 mL of deoxygenated water and the resulting solution was slowly added to the cerium nitrate solution under stirring under a blanket of N_2. A yellow-brown precipitate appeared at the first drops, followed by a yellow gel and a grey gel and finally a violet suspension. The vessel was closed under N_2 and let to react during 30 min at r.t. and was then put in a preheated electric oven at 100 °C for 20 h. After reaction, the solution was let to cool down naturally to r.t. A grey powder sedimented at the bottom of the vessel, the supernatant was colorless. The solution was centrifugated under air. The powder was washed 6 times with 30 mL of H_2O and once with 30 mL of EtOH. The obtained grey powder (326 mg, 95 % yield) was then dried under N_2 and stored under argon. One should note that extended reaction times at high pH in contact with borosilicate glass may lead to a leaching of silicon species, which might be incorporated in the cerium oxide phase.[25] In the present work, leached aluminosilicate phases were detected by XRD, as indicated in SI.

Aging of Ce(OH)₃. The Ce(OH)₃ powder was let in an open glass vial at 20 °C in air for at least 7 days. The powder gradually changed from grey to yellow, without loss of mass.

Powder X–Ray Diffraction (XRD). XRD measurements were performed on a Bruker D8 Advance diffractometer, using Cu Kα radiation at 1.5419 Å, with steps of 0.05° and a scanning rate of 3 s/step. *In situ* thermodiffraction measurements were performed on a Bruker Discover diffractometer, using Cu Kα radiation at 1.5419 Å, with steps of 0.08° and a scanning rate of 2.4 s/step. Scans were collected every 5 °C during temperature plateaus of

30 min, *i.e.* with an average heating ramp of 10 °C/h. Backgrounds of the patterns are subtracted using the EVA software. High quality XRD measurements were performed at SOLEIL synchrotron on CRISTAL beamline in 0.5 mm diameter borosilicate capillaries (transmission mode) at an energy of 18.466 keV ($\lambda = 0.6714$ Å) using a MYTHEN2 X 9K detector (DECTRIS).

Neutron diffraction. Neutron powder diffraction data were collected on the high-resolution powder diffractometer Echidna at the OPAL research reactor, ANSTO, Australia.[26] Polycrystalline samples were loaded into 6 mm diameter cylindrical vanadium cans and the measurements were carried out at room temperature using neutrons of the wavelength $\lambda = 1.622$ Å.

The Rietveld refinements were performed using the FullProf Suite.[27]

DFT calculations. *Ab initio* DFT calculations were performed using the Vienna Ab initio Simulation Package (VASP, version 6.2.1),[28] as implemented in the MedeA environment.[29] Both the generalized gradient approximation (GGA) of Perdew, Burke, and Ernzerhof,[30] and several van der Waals functionals (rev-vdW-DF2[31] and rPW86-vdW2[32]) were tested and all showed consistent results. Since one of the two models contained molecular H_2O, it was important to test the effect of van der Waals corrections. Our choice was based on a previous work on hydrates.[33] The calculations for $CeO(OH)_2$ and $CeO_2(H_2O)$ showed that the difference in energy between the two models was much larger that the effect of the tested vdW corrections. The calculations were done without spin polarisation, since its energy scale is in the meV range, while the difference in energy between the two models was clearly several orders of magnitude larger, ~1 eV/unit cell, as indicated in the text. A Γ-point centered 5x7x5 k-point mesh with the Gaussian smearing method and smearing width of 0.05 eV was used with a plane-wave energy cutoff of 500 eV. Optimization of the atomic positions

with the unit cell fixed to the experimental values was carried out using the conjugate gradient algorithm with 0.02 eV/Å convergence tolerance.

Transmission Electron Microscopy (TEM). A drop of a diluted solution of nanoparticles dispersed in ethanol was allowed to dry on an amorphous carbon coated copper grid. TEM images were acquired with a TWIN 120 (TECNAI SPIRIT) operating at 120 kV.

X–ray Absorption Spectroscopy (XAS). Ce L_{III}-edge XAS data were collected at the LUCIA beamline at synchrotron SOLEIL, with an electron energy of 2.7 GeV and an average ring current of 450 mA. The incoming photons were selected with a Si (111) double-crystal monochromator. A 3 mg portion of the sample was diluted in *ca.* 40 mg of graphite and was compressed to form a 6 mm diameter pellet. During typical analyses, the pressure in the chamber was maintained around 10^{-2} mbar. Measurements were performed in fluorescence mode using a Bruker silicon drift detector, with an outgoing photon angle of 2°. A beam size of 2 x 4 mm (v x h) was used and radiation damage effects were carefully monitored by collecting several consecutive spectra and ensuring reproducibility. Data analysis was carried out using the Athena software.[34]

Fourier Tranform Infrared Spectroscopy. Infrared spectra were collected on a Spectrum 400 (PERKINELMER) spectrometer. The dry sample (1−3 mg) was deposited on an attenuated total reflectance (ATR) crystal. Transmittance was measured between 4000 and 550 cm^{-1} with steps of 0.5 cm^{-1}.

Author contributions

R. F. A. conducted the syntheses, the characterizations and the data treatment. G. R. performed the Rietveld refinements and the crystallography analysis. C. S. participated to the thermodiffraction data acquisition, treatment and analysis. M. A. performed the neutron diffraction measurement and the DFT calculations. B. L.-K. performed the XAS

measurements. B.B. participated to the XRD data acquisition on CRISTAL. R. F. A., G. R. and S. C. conceived the project and co-wrote the manuscript, S. C. spearheading it. All authors approved the final version of the manuscript.

Conflict of interest

The authors declare no conflict of interest.

Supporting information

Additional tables and figures as to CeO_2 synthesis and optimization of $Ce(OH)_3$ purity, beam damage effects, electron diffraction data, extended structure of $Ce(OH)_3$, representative diffractograms during thermodiffraction and IR spectra after calcination.

Acknowledgements

References

(1)   Montini, T.; Melchionna, M.; Monai, M.; Fornasiero, P. Fundamentals and Catalytic Applications of CeO_2-Based Materials. *Chem. Rev.* **2016**, *116* (10), 5987–6041. https://doi.org/10.1021/acs.chemrev.5b00603.

(2)   TROVARELLI, A. Catalytic Properties of Ceria and CeO_2-Containing Materials. *Catal. Rev.* **1996**, *38* (4), 439–520. https://doi.org/10.1080/01614949608006464.

(3)   Vilé, G.; Wrabetz, S.; Floryan, L.; Schuster, M. E.; Girgsdies, F.; Teschner, D.; Pérez-Ramírez, J. Stereo- and Chemoselective Character of Supported CeO_2 Catalysts for Continuous-Flow Three-Phase Alkyne Hydrogenation. *ChemCatChem* **2014**, *6* (7), 1928–1934. https://doi.org/10.1002/cctc.201402124.

(4)   Mai, H.-X.; Sun, L.-D.; Zhang, Y.-W.; Si, R.; Feng, W.; Zhang, H.-P.; Liu, H.-C.; Yan, C.-H. Shape-Selective Synthesis and Oxygen Storage Behavior of Ceria Nanopolyhedra, Nanorods, and Nanocubes. *J. Phys. Chem. B* **2005**, *109* (51), 24380–24385. https://doi.org/10.1021/jp055584b.

(5)   Li, J.; Zhang, Z.; Gao, W.; Zhang, S.; Ma, Y.; Qu, Y. Pressure Regulations on the Surface Properties of CeO 2 Nanorods and Their Catalytic Activity for CO Oxidation and Nitrile Hydrolysis Reactions. *ACS Appl. Mater. Interfaces* **2016**, *8* (35), 22988–22996. https://doi.org/10.1021/acsami.6b05343.

(6)   Ivanov, V. K.; Shcherbakov, A. B.; Usatenko, A. V. Structure-Sensitive Properties and Biomedical Applications of Nanodispersed Cerium Dioxide. *Russ. Chem. Rev.* **2009**, *78* (9), 855–871. https://doi.org/10.1070/RC2009v078n09ABEH004058.

(7)   Yang, C.; Lu, Y.; Zhang, L.; Kong, Z.; Yang, T.; Tao, L.; Zou, Y.; Wang, S. Defect Engineering on CeO_2-Based Catalysts for Heterogeneous Catalytic Applications. *Small Struct.* **2021**, *2* (12), 2100058. https://doi.org/10.1002/sstr.202100058.

(8)   Xu, Y.; Mofarah, S. S.; Mehmood, R.; Cazorla, C.; Koshy, P.; Sorrell, C. C. Design

Strategies for Ceria Nanomaterials: Untangling Key Mechanistic Concepts. *Mater. Horizons* **2021**, *8* (1), 102–123. https://doi.org/10.1039/D0MH00654H.

(9)   Wang, R.; Dangerfield, R. Seed-Mediated Synthesis of Shape-Controlled CeO_2 Nanocrystals. *RSC   Adv.   **2014**,   4   (7),   3615–3620.* https://doi.org/10.1039/C3RA44495C.

(10)   Abi-aad, E.; Bechara, R.; Grimblot, J.; Aboukais, A. Preparation and Characterization of Ceria under an Oxidizing Atmosphere. Thermal Analysis, XPS, and EPR Study. *Chem. Mater.* **1993**, *5* (6), 793–797. https://doi.org/10.1021/cm00030a013.

(11)   Balasubramanian, M.; Melendres, C. .; Mansour, A. . An X-Ray Absorption Study of the Local Structure of Cerium in Electrochemically Deposited Thin Films. *Thin Solid Films* **1999**, *347* (1–2), 178–183. https://doi.org/10.1016/S0040-6090(98)01754-4.

(12)   Balasubramanian, M.; Melendres, C. A.; Mansour, A. N. X-Ray Absorption Spectroscopy Study of the Local Structure of Heavy Metal Ions Incorporated into Electrodeposited Nickel Oxide Films. *J. Electrochem. Soc.* **1999**, *146* (2), 607–614. https://doi.org/10.1149/1.1391651.

(13)   Mullica, D. F.; Oliver, J. D.; Milllgan, W. O. Cerium Trihydroxide. *Acta Crystallogr. Sect. B Struct. Crystallogr. Cryst. Chem.* **1979**, *35* (11), 2668–2670. https://doi.org/10.1107/S0567740879010104.

(14)   Zhang, S.; Huang, Z.; Ma, Y.; Gao, W.; Li, J.; Cao, F.; Li, L.; Chang, C.; Qu, Y. Solid Frustrated-Lewis-Pair Catalysts Constructed by Regulations on Surface Defects of Porous Nanorods of CeO_2. *Nat. Commun.* **2017**, *8* (May), 1–11. https://doi.org/10.1038/ncomms15266.

(15)   Carpenter, J. H. New Measurements of Oxygen Solubility in Pure and Natural Water. *Limnol. Oceanogr.* **1966**, *11* (2), 264–277. https://doi.org/10.4319/lo.1966.11.2.0264.

(16)   Tang, C. C.; Bando, Y.; Liu, B. D.; Golberg, D. Cerium Oxide Nanotubes Prepared

from Cerium Hydroxide Nanotubes. *Adv. Mater.* **2005**, *17* (24), 3005–3009. https://doi.org/10.1002/adma.200501557.

(17)   Li, J.; Zhang, Z.; Tian, Z.; Zhou, X.; Zheng, Z.; Ma, Y.; Qu, Y. Low Pressure Induced Porous Nanorods of Ceria with High Reducibility and Large Oxygen Storage Capacity: Synthesis and Catalytic Applications. *J. Mater. Chem. A* **2014**, *2* (39), 16459–16466. https://doi.org/10.1039/C4TA03718A.

(18)   Shahin, A. M.; Grandjean, F.; Long, G. J.; Schuman, T. P. Cerium L III -Edge XAS Investigation of the Structure of Crystalline and Amorphous Cerium Oxides. *Chem. Mater.* **2005**, *17* (2), 315–321. https://doi.org/10.1021/cm0492437.

(19)   Stokes, H. T.; Hatch, D. M.; Campbell, B. J. ISODISTORT, ISOTROPY Software Suite, Iso.Byu.Edu.

(20)   Campbell, B. J.; Stokes, H. T.; Tanner, D. E.; Hatch, D. M. ISODISPLACE : A Web-Based Tool for Exploring Structural Distortions. *J. Appl. Crystallogr.* **2006**, *39* (4), 607–614. https://doi.org/10.1107/S0021889806014075.

(21)   Ajmal, M.; Ali, T.; Adil Khan, M.; Ahmad, S.; Ahmad Mian, S.; Waheed, A.; Ali, S. Structural and Optical Properties of $La_2O_3:Ho^{3+}$ and $La(OH)_3:Ho^{3+}$ Crystalline Particles. *Mater. Today Proc.* **2017**, *4* (3), 4900–4905. https://doi.org/10.1016/j.matpr.2017.04.093.

(22)   Weltner, W.; DeKock, R. L. Spectroscopy of Rare Earth Oxide Molecules in Inert Matrices at 4 K. *J. Phys. Chem.* **1971**, *75* (4), 514–525. https://doi.org/10.1021/j100674a013.

(23)   Bozon-Verduraz, F.; Bensalem, A. IR Studies of Cerium Dioxide: Influence of Impurities and Defects. *J. Chem. Soc. Faraday Trans.* **1994**, *90* (4), 653. https://doi.org/10.1039/ft9949000653.

(24)   Vayssilov, G. N.; Mihaylov, M.; Petkov, P. St.; Hadjiivanov, K. I.; Neyman, K. M.

Reassignment of the Vibrational Spectra of Carbonates, Formates, and Related Surface Species on Ceria: A Combined Density Functional and Infrared Spectroscopy Investigation. *J. Phys. Chem. C* **2011**, *115* (47), 23435–23454. https://doi.org/10.1021/jp208050a.

(25) Gennari, F. C.; Montini, T.; Hickey, N.; Fornasiero, P.; Graziani, M. IR Investigation of the Interaction of Deuterium with $Ce_{0.6}Zr_{0.4}O_2$ and Cl-Doped $Ce_{0.6}Zr_{0.4}O_2$. *Appl. Surf. Sci.* **2006**, *252* (24), 8456–8465. https://doi.org/10.1016/j.apsusc.2005.11.062.

(26) Avdeev, M.; Hester, J. R. ECHIDNA: A Decade of High-Resolution Neutron Powder Diffraction at OPAL. *J. Appl. Crystallogr.* **2018**, *51* (6), 1597–1604. https://doi.org/10.1107/S1600576718014048.

(27) Rodríguez-Carvajal, J. Recent Advances in Magnetic Structure Determination by Neutron Powder Diffraction. *Phys. B Condens. Matter* **1993**, *192* (1–2), 55–69. https://doi.org/10.1016/0921-4526(93)90108-I.

(28) Kresse, G.; Furthmüller, J. Efficient Iterative Schemes for Ab Initio Total-Energy Calculations Using a Plane-Wave Basis Set. *Phys. Rev. B* **1996**, *54* (16), 11169–11186. https://doi.org/10.1103/PhysRevB.54.11169.

(29) *MedeA 3.6;* MedeA Is a Registered Trademark of Materials Design, Inc., San Diego, USA.

(30) Perdew, J. P.; Burke, K.; Ernzerhof, M. Generalized Gradient Approximation Made Simple. *Phys. Rev. Lett.* **1996**, *77* (18), 3865–3868. https://doi.org/10.1103/PhysRevLett.77.3865.

(31) Hamada, I. Van Der Waals Density Functional Made Accurate. *Phys. Rev. B* **2014**, *89* (12), 121103. https://doi.org/10.1103/PhysRevB.89.121103.

(32) Lee, K.; Murray, É. D.; Kong, L.; Lundqvist, B. I.; Langreth, D. C. Higher-Accuracy van Der Waals Density Functional. *Phys. Rev. B* **2010**, *82* (8), 081101.

https://doi.org/10.1103/PhysRevB.82.081101.

(33) Peets, D. C.; Avdeev, M.; Rahn, M. C.; Pabst, F.; Granovsky, S.; Stötzer, M.; Inosov, D. S. Crystal Growth, Structure, and Noninteracting Quantum Spins in Cyanochroite, $K_2Cu(SO_4)_2 \cdot 6H_2O$. *ACS Omega* **2022**, *7* (6), 5139–5145. https://doi.org/10.1021/acsomega.1c06143.

(34) Ravel, B.; Newville, M. ATHENA , ARTEMIS , HEPHAESTUS : Data Analysis for X-Ray Absorption Spectroscopy Using IFEFFIT. *J. Synchrotron Radiat.* **2005**, *12* (4), 537–541. https://doi.org/10.1107/S0909049505012719.

TOC Graphic